# FRET Networks: Modeling and Analysis for Computing


**Masaki Nakagawa**

**Abstract** FRET networks, which refer to energy transfer networks between nanoparticles due to Förster resonance energy transfer (FRET), are promising physical phenomena for realizing high-speed, efficient, and compact information processing. These networks can generate rich spatiotemporal signals that help in information processing and are capable of function approximation, time-series prediction, and pattern recognition. This chapter presents a mathematical model and analysis for FRET networks, including some simulation methods for the model, and demonstrates the power of FRET networks for information processing.

## 1 Introduction

The energy transfer caused by dipole–dipole interactions between fluorescent molecules is known as Förster resonance energy transfer (FRET). Förster theory [1] states the energy transfer rate (the expected number of energy transferred per unit time) to be such that

$$k^{\mathrm{FRET}} = \frac{3}{2}\frac{\kappa^2}{\tau}\left(\frac{R_0}{r}\right)^6, \tag{1}$$

where $\kappa$ is an orientation factor, $\tau$ is a natural excited-state lifetime, $R_0$ is the Förster distance, and $r$ is the distance between fluorescent molecules. This relation shows that the energy transfer rate sensitively depends on the distance $r$ between fluorescent molecules as it is proportional to $r$ to the power of $-6$.

Consider randomly distributing a large number of fluorescent molecules. The fluorescent molecules are separated by various distances. Therefore, the energies on the network are transferred through diverse pathways. If time-series signals are input as excitation light in the network, we can expect high-dimensionalized and nonlinearized time-series signals to be produced as fluorescence. Furthermore, we

M. Nakagawa (✉)
Fukuoka Institute of Technology, 3-30-1 Wajiro-higashi, Higashi-ku, Fukuoka 811-0295, Japan
e-mail: m-nakagawa@fit.ac.jp



H. Suzuki et al. (eds.), *Photonic Neural Networks with Spatiotemporal Dynamics*,
https://doi.org/10.1007/978-981-99-5072-0_6

can expect some memory of previous input to be left in the network because input energy cycles to some extent in the network. Therefore, this energy transfer network due to FRET can be a prominent phenomenon toward a novel information processing device.

FRET has been used as local nanoscale signaling without molecular diffusion processes. For example, local signaling by FRET between fluorescent molecules on DNA substrates is used as photonic logic gates [2–5]. As previously stated, the kinetics of single-step FRET is well explained by Förster theory, even in special environments such as membranes and solutions (see Chaps. 13–15 in [1]). Furthermore, the kinetics of multistep FRET (a cascade of FRET) can also be understood in principle using Förster theory. Multistep FRET has been demonstrated experimentally on linear DNA scaffolds using heterogeneous fluorescent dyes [6] and even homogeneous fluorescent dyes [7]. Furthermore, multistep FRET occurs also in hetero- and homogeneous quantum dots (QDs) [8, 9]. If spatially distributed fluorescent molecules are excited simultaneously, multistep FRET can occur over multiple locations and times, where fluorescent molecules act as both donors and acceptors depending on temporally changing situations. This multistep FRET network is the one we will consider in the study.

The spatiotemporal dynamics of FRET networks are very important from an information processing perspective. For example, the spatiotemporal dynamics of multistep FRET have been used to design intelligent system components, such as unclonable physical keys [10] and photonic logic gates [2–5]. Some FRET networks on spatially distributed QDs are shown to generate diverse spatiotemporal signals that can be used for information processing [11]. The key to designing information-processing applications for FRET networks is to understand the spatiotemporal behavior of FRET networks. In our previous paper [12], we developed a spatiotemporal mathematical model for FRET networks and revealed its temporal characteristic behavior. We emphasize that our model applies to any fluorescent molecule. However, we concentrate on QD-based FRET networks because QDs are expected to be important fundamental elements in realizing compact and energy-efficient information-processing systems [13–16].

The rest of this chapter is organized as follows: In Sect. 2, we introduce a spatiotemporal model for FRET networks, called the multiple-donor model, and show various analytical (theoretical) results. Section 3 presents some FRET network simulation methods, from deterministic to stochastic ones, and compares deterministic and stochastic methods to reveal the pros and cons of both methods. In Sect. 4, we show the power of FRET networks for information processing by simulations, particularly nonlinear function approximation, chaotic time-series prediction, and handwritten digit recognition. Finally, we summarize this chapter and mention some future works in Sect. 5.

## 2 Spatiotemporal Model for FRET Networks

In this section, we first introduce a spatiotemporal mathematical model for FRET networks. Then, we show some analytical results for the model. The first part of this section almost follows our previous paper [12].

### *2.1 Multiple-Donor Model*

Wang et al. [17, 18] developed a mathematical model to describe the dynamics of multistep FRET that assumes networks with *no more than one* excited molecule, which we refer to as the "single-donor model." The single-donor model is a continuous-time Markov chain (CTMC) with a finite or countable state space where the time spent in each state is exponentially distributed. The single-donor model assumes that the system has only one excited molecule and hence, cannot consider the "level occupancy effect," which means that already excited molecules are effectively forbidden from energy absorption. However, the level occupancy effect is essential for FRET networks because they involve multiple excited molecules (donors) and non-excited molecules (acceptors). The "multiple-donor model" [12] is an extended version of the single-donor model that assumes networks with multiple excited molecules and non-excited molecules. Although similar models that consider the level occupancy effect already exist [19, 20], their approaches differ from ours in the following points: (i) Their main aim is to present a Monte Carlo simulation algorithm using their models. On the contrary, our main aim is to produce the theoretical results using our model and thus understand the spatiotemporal behavior fundamentally. (ii) They introduce the level occupancy effect as the complete exclusion of already excited molecules from their roles as acceptors, whereas our model incorporates such roles by considering the Auger recombination. (iii) Their models mainly handle the decay processes, whereas our model additionally covers the light-induced excitation process.

In the multiple-donor model for the system consisting of $N$ QDs, we first represent the system state by an element in $\{0, 1\}^N$, where each QD is assigned either a ground state "0" or an excited state "1." Then, we consider the system state probability $P_{i_1 \dots i_N}(t)$ such that the system is in $(i_1, i_2, \dots, i_N) \in \{0, 1\}^N$ at time $t$, where $i_n$ represents the $n$th QD's state, 0 or 1. Evidently, $0 \leq i_1 + i_2 + \cdots + i_N \leq N$. It should hold that $\sum_{(i_1,\dots,i_N)\in\{0,1\}^N} P_{i_1 \dots i_N}(t) = 1$ for all $t \in \mathbb{R}$. As we consider the whole system state at each time, we can consider the level occupancy effect in FRET between QDs, as shown later.

Next, we define the state transition rules between system states $(i_1, \dots, i_N)$. The following symbols are used:

$$S_n = (i_1, \dots, i_{n-1}, 0, i_{n+1}, \dots, i_N),$$
$$S_n^* = (i_1, \dots, i_{n-1}, 1, i_{n+1}, \dots, i_N).$$

The state transition rules consist of the following five rules in the multiple-donor model:

$$S_n^* \xrightarrow{k_n^{\mathrm{F}}} S_n, \tag{2a}$$

$$S_n^* \xrightarrow{k_n^{\mathrm{N}}} S_n, \tag{2b}$$

$$S_n^* + S_m \xrightarrow{k_{nm}^{\mathrm{FRET}}} S_n + S_m^*, \tag{2c}$$

$$S_n^* + S_m^* \xrightarrow{k_{nm}^{\mathrm{FRET}}} S_n + S_m^*, \tag{2d}$$

$$S_n \xrightarrow{k_n^{\mathrm{E}}(t)} S_n^*, \tag{2e}$$

where $k_n^{\mathrm{F}}$ and $k_n^{\mathrm{N}}$ denote the rate constants of radiative (fluorescence) decay and nonradiative decay for the $n$th QD, respectively, and $k_{nm}^{\mathrm{FRET}}$ denotes the rate constant of FRET from the $n$th QD to the $m$th QD. $k_n^{\mathrm{E}}(t)$ denotes the rate constant of the excitation process with irradiation of time-dependent excitation light for the $n$th QD. The time spent in each state is exponentially distributed with each rate constant, $k_n^{\mathrm{F}}$, $k_n^{\mathrm{N}}$, $k_{nm}^{\mathrm{FRET}}$, or $k_n^{\mathrm{E}}(t)$. We also illustrate the state transition rules (2a–2e) in Fig. 1.

The rate constants in the state transition rules (2a–2e) are given using the fundamental physical constants as follows:

$$k_n^{\mathrm{F}} = Q_n/\tau_n, \tag{3a}$$

$$k_n^{\mathrm{N}} = (1 - Q_n)/\tau_n, \tag{3b}$$

$$k_{nm}^{\mathrm{FRET}} = (3/2)\left(\kappa_{nm}^2/\tau_n\right)\left(R_{nm}/r_{nm}\right)^6, \tag{3c}$$

$$k_n^{\mathrm{E}}(t) = \sigma_n I_{\mathrm{ex},n}(t), \tag{3d}$$

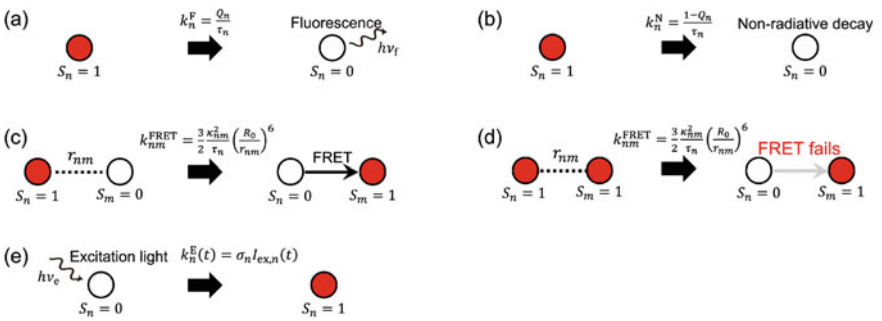


**Fig. 1** State transitions in the multiple-donor model: (**a**) Deactivation due to fluorescence, (**b**) Non-radiative deactivation, (**c**) Excitation–deactivation due to FRET, (**d**) Deactivation due to the level occupancy effect, and (**e**) Excitation due to light-induced excitation. Note that $h\nu_{(\mathrm{f})}$, $h\nu_{(\mathrm{e})}$ denote a fluorescence photon and an excitation photon, respectively

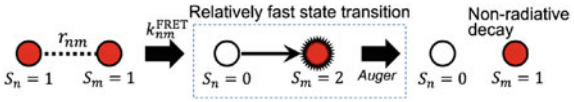


**Fig. 2** Auger recombination in the process of two excited-QDs interactions. Since Auger recombination is a fast process, the resulting state transition follows Rule (2d)

where $Q_n$, $\tau_n$ denote the quantum yield and the natural excited-state lifetime for the $n$th QD, respectively. $\kappa_{nm}^2$ is the orientation factor between the $n$th and $m$th QDs. $R_{nm}$ and $r_{nm}$ denote the Förster and physical distances from the $n$th QD to the $m$th QD, respectively. $\sigma_n$ denotes the collision cross section for the $n$th QD, and $I_{\mathrm{ex},n}(t)$ denotes the irradiation photon density for the $n$th QD.

We note that the transition rules (2a–2c) are essentially equivalent to the ones of the single-donor model [17, 18]. On the other hand, the transition rules (2d–2e) are originally introduced in our study [12]. Rule (2d) describes an energy transfer by FRET and the subsequent Auger recombination. The Auger recombination is a nonradiative decay process from a higher energy excitation state $S_m^{**} = (i_1, \ldots, i_{m-1}, 2, i_{m+1}, \ldots, i_N)$ to the first level excitation state $S_m^*$. Although the Auger recombination can be modeled as several interactions [21], we will assume here for simplicity that this decay process is relatively rapid, i.e., $S_m^{**} \overset{\infty}{\longrightarrow} S_m^*$ (see Fig. 2). Therefore, the resulting state transition follows Rule (2d). Finally, Rule (2e) is the state transition due to the light-induced excitation process.

For simplicity, we assume that the orientation factors $\kappa_{nm}^2$ and physical distances $r_{nm}$ are constant in time, i.e., QDs have low anisotropies and minimal lateral motions during their excited-state lifetimes. Our model can also be applied to such situations for (i) orientation factor values other than the commonly assumed $2/3$ or even dynamic ones and (ii) diffusion of QDs during their excited states. However, when a considerably faster rotation or diffusion compared to their excited-state lifetimes is considered, one may need to use simpler models (see Chap. 4 in [22] or [23] for the dynamic averaging regime and [24] for the rapid-diffusion limit).

Considering the inflow and outflow of probability, the master equation of the multiple-donor model defined by the state transition rules (2a–2d) is given as follows:

$$\begin{aligned}\frac{\mathrm{d}}{\mathrm{d}t} P_{i_1 \cdots i_N}(t) = &- \sum_{n=1}^{N} i_n (k_n^{\mathrm{F}} + k_n^{\mathrm{N}}) P_{i_1 \cdots i_N}(t) \\ &+ \sum_{n=1}^{N} \bar{i}_n (k_n^{\mathrm{F}} + k_n^{\mathrm{N}}) \mathcal{S}_n^{+} P_{i_1 \cdots i_N}(t) - \sum_{n,m=1}^{N} i_n k_{nm}^{\mathrm{FRET}} P_{i_1 \cdots i_N}(t) \\ &+ \sum_{n,m=1}^{N} \bar{i}_n i_m k_{nm}^{\mathrm{FRET}} \mathcal{S}_n^{+} P_{i_1 \cdots i_N}(t) + \sum_{n,m=1}^{N} \bar{i}_n i_m k_{nm}^{\mathrm{FRET}} \mathcal{S}_n^{+} \mathcal{S}_m^{-} P_{i_1 \cdots i_N}(t)\end{aligned}$$

$$-\sum_{n=1}^{N} \bar{i}_n k_n^{\mathrm{E}}(t) P_{i_1 \cdots i_N}(t) + \sum_{n=1}^{N} i_n k_n^{\mathrm{E}}(t) \mathcal{S}_n^{-} P_{i_1 \cdots i_N}(t), \tag{4}$$

where $\bar{i}_n$ denotes the inverted binary for the $n$th QD's state $i_n$, i.e., $\bar{i}_n = 1 - i_n$, and $\mathcal{S}_n^{\pm}$ denotes the shift operator for states $(i_1, \ldots, i_N)$, i.e., $\mathcal{S}_n^{\pm} P_{i_1 \ldots i_n \ldots i_N}(t) = P_{i_1 \ldots i_n \pm 1 \ldots i_N}(t)$. Notably, if the state $(i_1, \ldots, i_n \pm 1, \ldots, i_N)$ is improper, i.e., not in $\{0, 1\}^N$, $P_{i_1 \ldots i_n \pm 1 \ldots i_N}(t) = 0$. In addition, we set $k_{nn}^{\mathrm{FRET}} = 0$. The time-dependent fluorescence intensity $I(t)$ is expressed as

$$I(t) = \sum_{(i_1, \ldots, i_N) \in \{0,1\}^N} \left[ \sum_{n=1}^{N} i_n k_n^{\mathrm{F}} P_{i_1 \ldots i_N}(t) \right]. \tag{5}$$

Note that the master equation (4) includes spatial information through the rate constants $k_{nm}^{\mathrm{FRET}}$ (i.e., the network structure of QDs). In the following sections, we focus on the temporal behavior of the FRET network and analyze our model and also the single-donor model.

As mentioned earlier, the single-donor model assumes networks with *at most one* excited molecule [17, 18]. Namely, only the state transition rules described in (2a–2c) are considered. Therefore, the master equation of the single-donor model is as follows:

$$\frac{\mathrm{d}}{\mathrm{d}t} P_n(t) = -(k_n^{\mathrm{F}} + k_n^{\mathrm{N}}) P_n(t) - \sum_{m=1}^{N} k_{nm}^{\mathrm{FRET}} P_n(t) + \sum_{m=1}^{N} k_{mn}^{\mathrm{FRET}} P_m(t), \tag{6}$$

where $P_n(t)$ denotes the probability that the $n$th QD is in an excited state.

Now, we will show that the master equation (4) of the multiple-donor model coincides with the master equation (6) of the single-donor model if we assume networks with no excitation light and only one excited molecule, i.e., $k_n^{\mathrm{E}} = 0$ and $i_1 + \cdots + i_N \leq 1$. To show this, let us assume $i_1 + \cdots + i_N \leq 1$ and put $P_{0 \ldots 1 \ldots 0}^{\ \ n}(t) = P_n(t)$ in (4). Then, one can easily transform each term in the right-hand side of (4) as follows: (the first term) $= -(k_n^{\mathrm{F}} + k_n^{\mathrm{N}}) P_n(t)$, (the second term) $= 0$, (the third term) $= -\sum_{m=1}^{N} k_{nm}^{\mathrm{FRET}} P_n(t)$, (the fourth term) $= 0$, (the fifth term) $= \sum_{m=1}^{N} k_{mn}^{\mathrm{FRET}} \mathcal{S}_m^{+} \mathcal{S}_n^{-} P_n(t) = \sum_{m=1}^{N} k_{mn}^{\mathrm{FRET}} P_m(t)$, (the sixth term) $= 0$, (the seventh term) $= 0$.

## 2.2 Analytical Results

### 2.2.1 Multicomponent Exponential Decay

Here, we present the fundamental temporal property of the decay process of the fluorescence intensity derived from the multiple-donor model with $k^{\mathrm{E}}(t) = 0$. We show

that nontrivial network-induced properties of fluorescence intensity decay occur when multiple donors are considered. The derivation will almost follow our previous paper [12], except for the expression of some formulae.

Now consider the simplest situation where the network consists of only one type of QDs, i.e., $k_n^{\mathrm{F}} = k^{\mathrm{F}}$, $k_n^{\mathrm{N}} = k^{\mathrm{N}}$, $k^{\mathrm{F}} + k^{\mathrm{N}} = 1/\tau$ for all $n$, and $k_{nm}^{\mathrm{FRET}} = k_{mn}^{\mathrm{FRET}}$ for all $n, m$.

First, we will show that the single-donor model (6) implies the single-exponential decay. Because the fluorescence intensity in the single-donor model (6) becomes $I(t) = k^{\mathrm{F}} \sum_{n=1}^{N} P_n(t)$, the derivative of $I(t)$ becomes

$$\frac{\mathrm{d}}{\mathrm{d}t} I(t) = -\frac{1}{\tau} I(t) - \sum_{n,m=1}^{N} k_{nm}^{\mathrm{FRET}} k^{\mathrm{F}} P_n(t) + \sum_{n,m=1}^{N} k_{mn}^{\mathrm{FRET}} k^{\mathrm{F}} P_m(t). \tag{7}$$

The sum of the second and third terms on the right-hand side of (7) is zero because of the symmetricity of $k_{nm}^{\mathrm{FRET}}$. Therefore, the single-donor model (6) implies the single-exponential decay, i.e., $I(t) = I(0) \exp(-t/\tau)$.

Next, we will show that the multiple-donor model (4) implies the multicomponent exponential decay, i.e., $I(t) = \sum_j \alpha_j \exp(-t/\tau_j)$. To show this, we define the $l$-excited states as

$$\Lambda_l = \{(i_1, \ldots, i_N) \in \{0, 1\}^N : i_1 + \cdots + i_N = l\}$$

and the time-dependent fluorescence intensity from the $l$-excited states as follows:

$$I_l(t) = \sum_{(i_1,\ldots,i_N)\in\Lambda_l} \left[ \sum_{n=1}^{N} i_n k_n^{\mathrm{F}} P_{i_1 \ldots i_N}(t) \right]. \tag{8}$$

Obviously, $I(t) = \sum_{l=1}^{N} I_l(t)$ holds from (5) and (8). The following expression for the all-excited-state probability $P_{1\ldots1}(t)$ can be easily derived from (4) in the case where the network consists of only one type of QDs:

$$\frac{\mathrm{d}}{\mathrm{d}t} P_{1\ldots1}(t) = -\frac{N}{\tau} P_{1\ldots1}(t) - \left( \sum_{n,m=1}^{N} k_{nm}^{\mathrm{FRET}} \right) P_{1\ldots1}(t). \tag{9}$$

Therefore, the all-excited-state probability $P_{1\ldots1}(t)$ shows the single-exponential decay as follows:

$$P_{1\ldots1}(t) = P_{1\ldots1}(0) \exp\left( -\frac{t}{\tau_*^{(N)}} \right), \quad \tau_*^{(N)} = \left( \frac{N}{\tau} + \sum_{n,m=1}^{N} k_{nm}^{\mathrm{FRET}} \right)^{-1}. \tag{10}$$

Because $I_N(t) = Nk^{\mathrm{F}} P_{1\ldots1}(t)$, the resulting fluorescence intensity $I_N(t)$ also shows the single-exponential decay $I_N(t) = I_N(0)\exp\left(-t/\tau_*^{(N)}\right)$. Similarly, the following expression for the $(N-1)$-excited-state probability $P_{1\ldots\overset{n}{0}\ldots1}(t)$ can be derived from (4) by a straightforward calculation:

$$\frac{\mathrm{d}}{\mathrm{d}t} P_{1\ldots\overset{n}{0}\ldots1}(t) = \sum_{m=1}^{N} A_{nm} P_{1\ldots\overset{m}{0}\ldots1}(t) + \left(\frac{N}{\tau} + \sum_{m=1}^{N} k_{nm}^{\mathrm{FRET}}\right) P_{1\ldots1}(t), \tag{11}$$

where the elements of the matrix $A$ are

$$A_{nm} = -\left(\frac{N-1}{\tau} + \sum_{\substack{n',m'=1 \\ (n'\neq n)}}^{N} k_{n'm'}^{\mathrm{FRET}}\right)\delta_{nm} + k_{nm}^{\mathrm{FRET}}(1-\delta_{nm}). \tag{12}$$

$\delta_{nm}$ denotes the Kronecker delta. Since matrix $A$ is real symmetric, it has real eigenvalues and can be diagonalized. Let $\lambda_1, \ldots, \lambda_N$ be the real eigenvalues (with multiplicity) of the matrix $A$. One can show that the matrix $A$ is negative definite, i.e., $\mathbf{x}^{\mathrm{T}} A\mathbf{x} < 0$ for all nonzero $\mathbf{x} \in \mathbb{R}^N$, by a straightforward calculation and rearrangement of the terms:

$$\begin{aligned}
&\sum_{n,m=1}^{N} x_n A_{nm} x_m \\
&= -\frac{N-1}{\tau}\sum_{n=1}^{N} x_n^2 - \sum_{n=1}^{N}\left(\sum_{\substack{n',m'=1 \\ (n'\neq n)}}^{N} k_{n'm'}^{\mathrm{FRET}}\right) x_n^2 + \sum_{n,m=1}^{N} k_{nm}^{\mathrm{FRET}} x_n x_m \\
&= -\frac{N-1}{\tau}\sum_{n=1}^{N} x_n^2 - \sum_{n=1}^{N}\left(\sum_{\substack{n'<m' \\ (n',m'\neq n)}}^{N} 2k_{n'm'}^{\mathrm{FRET}}\right) x_n^2 - \sum_{n<m} k_{nm}^{\mathrm{FRET}}(x_n - x_m)^2 \quad < 0,
\end{aligned} \tag{13}$$

where we frequently used the symmetricity of $k_{nm}^{\mathrm{FRET}}$. Therefore, all of the eigenvalues $\lambda_j$ are strictly negative. Thus, one can see that the solution of (11), $P_{1\ldots\overset{n}{0}\ldots1}(t)$, is a linear sum of $\exp\left(-t/\tau_*^{(N-1,1)}\right)$, …, $\exp\left(-t/\tau_*^{(N-1,N)}\right)$ and $\exp\left(-t/\tau_*^{(N)}\right)$, where the decay times are $\tau_*^{(N-1,j)} = |\lambda_j|^{-1}$ labeled in ascending order. Because $I_{N-1}(t) = (N-1)k^{\mathrm{F}}\sum_{n=1}^{N} P_{1\ldots\overset{n}{0}\ldots1}(t)$, the resulting fluorescence intensity $I_{N-1}(t)$ shows the multicomponent exponential decay, including these exponential decay components. Finally, we will show that the fluorescence intensity $I_1(t)$ includes the exponential decay component $\exp(-t/\tau)$. The following expression for the 1-excited-state probability $P_{0\ldots\overset{n}{1}\ldots0}(t)$ can be derived from (4) by a straightforward

calculation:

$$\frac{\mathrm{d}}{\mathrm{d}t}P_{0\ldots1\ldots0}^{\ n}(t) = -\frac{1}{\tau}P_{0\ldots1\ldots0}^{\ n}(t) + \sum_{\substack{m=1\\(m\neq n)}}^{N}\left(\frac{1}{\tau}+k_{mn}^{\mathrm{FRET}}\right)P_{0\ldots1\ldots1\ldots0}^{\ n\ m}(t). \tag{14}$$

Therefore, the 1-excited-state probability $P_{0\ldots1\ldots0}^{\ n}(t)$ includes the exponential decay $\exp(-t/\tau)$ as $P_{0\ldots1\ldots1\ldots0}^{\ n\ m}(t)$ goes asymptotically to zero faster than $P_{0\ldots1\ldots0}^{\ n}(t)$. Because $I_1(t) = k^{\mathrm{F}}\sum_{n=1}^{N}P_{0\ldots1\ldots0}^{\ n}(t)$, the resulting fluorescence intensity $I_1(t)$ also includes the exponential decay component $\exp(-t/\tau)$. Note that we used a physical insight in the argument for (14); hence, it is not rigorous proof. In summary, the multiple-donor model (4) implies that the fluorescence intensity $I(t)$ shows the multicomponent exponential decay, including at least $N+2$ exponential decay components, i.e., $\exp\left(-t/\tau_*^{(N)}\right)$, $\exp\left(-t/\tau_*^{(N-1,1)}\right)$, …, $\exp\left(-t/\tau_*^{(N-1,N)}\right)$, and $\exp(-t/\tau)$ if $P_{1\ldots1}(0)\neq 0$ and $P_{1\ldots0\ldots1}^{\ n}(0)\neq 0$ for some $n$. We expect that each fluorescence intensity $I_l(t)$ from the $l$-excited states has potentially up to $\binom{N}{l}$ exponential decay components. Therefore, the resulting fluorescence intensity $I(t)$ has potentially up to $\sum_{l=1}^{N}\binom{N}{l} = 2^N - 1$ exponential decay components. Note that the observable number of exponential decay components can be smaller if fewer QDs are initially excited.

The above theoretical result, i.e., the appearance of multicomponent exponential decay even in single-type QDs, is qualitatively supported by experimental results obtained from spatially distributed single-type CdSe/ZnS QDs. See Sect. 3B in our previous study [12] for further details.

### 2.2.2 Some Analytical Results for Small QD Systems

We will show some analytical formulae for the fluorescence intensity in specific cases that assume equidistant QD systems, as shown in insets of Fig. 3. For other points, we continue to treat networks consisting of only one type of QDs and no excitation light. Let us introduce

$$\mathbf{P}(t) = \left[\mathbf{P}_{\Lambda_N}^{\mathsf{T}}\ \mathbf{P}_{\Lambda_{N-1}}^{\mathsf{T}}\ \ldots\ \mathbf{P}_{\Lambda_0}^{\mathsf{T}}\right]^{\mathsf{T}},$$

where $\mathbf{P}_{\Lambda_l}$ denotes a column vector consisting of $P_{i_1\ldots i_N}(t)$ for $(i_1,\ldots,i_N) \in \Lambda_l$, in which subscripts are in descending order as binary numbers. For example, when $N=2$, $\mathbf{P}(t) = [P_{11},\ P_{10},\ P_{01},\ P_{00}]^{\mathsf{T}}$, and when $N=3$, $\mathbf{P}(t) = [P_{111},\ P_{110},\ P_{101},\ P_{011}, P_{100},\ P_{010},\ P_{001}, P_{000}]^{\mathsf{T}}$. The master equation (4) in the multiple-donor model can also be expressed as

$$\frac{\mathrm{d}}{\mathrm{d}t}\mathbf{P}(t) = M(t)\mathbf{P}(t), \tag{15}$$

where $M(t)$ denotes the transition matrix with $2^N$ rows and $2^N$ columns for a $N$ QD system.

First, consider the simplest situation where the network consists of only one type of QDs and no excitation light. Then, the matrix $M$ in the case of $N = 2$ (see inset in Fig. 3(a)) becomes

$$M = \frac{1}{\tau}\begin{bmatrix} -2(\rho_r+1) & 0 & 0 & 0 \\ \rho_r+1 & -(\rho_r+1) & \rho_r & 0 \\ \rho_r+1 & \rho_r & -(\rho_r+1) & 0 \\ 0 & 1 & 1 & 0 \end{bmatrix} \quad \text{for } N = 2, \tag{16}$$

where $\rho_r = (R_0/r)^6$, and $r$ is the distance between two QDs.

Eigenvalue analysis using Maxima for the master equation (15) with the matrix (16) derives the fluorescence intensity decay of case $N = 2$, which has two exponential components:

$$I(t) = 2k^{\mathrm{F}}\frac{A_r}{2\rho_r+1}\exp\left(-\frac{2\rho_r+2}{\tau}t\right) + k^{\mathrm{F}}\frac{B_r}{2\rho_r+1}\exp\left(-\frac{1}{\tau}t\right) \quad \text{for } N = 2, \tag{17}$$

where $A_r = \rho_r P_{\Lambda_2}(0)$ and $B_r = 2(\rho_r+1)P_{\Lambda_2}(0) + (2\rho_r+1)P_{\Lambda_1}(0)$. We introduce initial state probabilities for $l$-excited states $\Lambda_l$:

$$P_{\Lambda_l}(0) = \sum_{(i_1,\ldots,i_N)\in\Lambda_l} P_{i_1\ldots i_N}(0).$$

We show the shape of (17) in Fig. 3(a).

In the same way, the matrix $M$ in the case of $N = 3$ (see inset in Fig. 3(b)) becomes

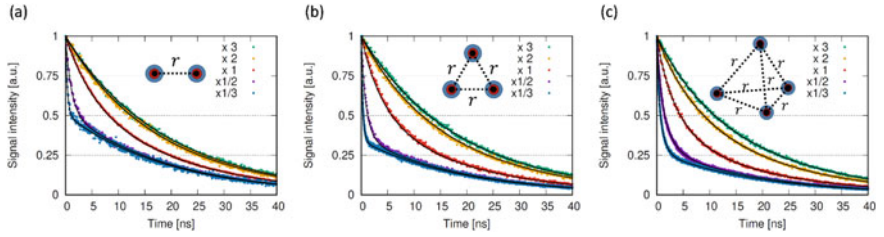


**Fig. 3** Analytical and numerical fluorescence intensity decay for equidistant QD systems: (**a**) 2QD, (**b**) 3QD, and (**c**) 4QD systems (see insets). Each color dot corresponds to each distance $r = c^{1/n} \times R_0$, $c = 3, 2, 1, 1/2$, and $1/3$, respectively, where Förster distance $R_0 = 6.18$ nm, and Dimension $n = 2$ for (**a**) and (**b**), $n = 3$ for (**c**). The solid black lines are analytical results obtained using (17), (19), and (20) for (**a**), (**b**), and (**c**), respectively. The dots are numerical results obtained from stochastic simulation, tRSSA, described in the next section

$$M = \frac{1}{\tau}\begin{bmatrix} A_{1\times 1} & \cdots & \cdots & O \\ B_{3\times 1} & C_{3\times 3} & \ddots & \vdots \\ \vdots & D_{3\times 3} & E_{3\times 3} & \vdots \\ O & \cdots & F_{1\times 3} & \vdots \end{bmatrix} \quad \text{for } N = 3, \tag{18}$$

where

$$A = -(6\rho_r + 3), \qquad B = \begin{bmatrix} 2\rho_r + 1 & 2\rho_r + 1 & 2\rho_r + 1 \end{bmatrix}^{\mathsf{T}},$$
$$C = \begin{bmatrix} -(4\rho_r + 2) & \rho_r & \rho_r \\ \rho_r & -(4\rho_r + 2) & \rho_r \\ \rho_r & \rho_r & -(4\rho_r + 2) \end{bmatrix}, \quad D = \begin{bmatrix} \rho_r + 1 & \rho_r + 1 & 0 \\ \rho_r + 1 & 0 & \rho_r + 1 \\ 0 & \rho_r + 1 & \rho_r + 1 \end{bmatrix},$$
$$E = \begin{bmatrix} -(2\rho_r + 1) & \rho_r & \rho_r \\ \rho_r & -(2\rho_r + 1) & \rho_r \\ \rho_r & \rho_r & -(2\rho_r + 1) \end{bmatrix}, \quad F = \begin{bmatrix} 1 & 1 & 1 \end{bmatrix}.$$

Eigenvalue analysis using Maxima for the master equation (15) with the matrix (18) derives the fluorescence intensity decay of case $N = 3$, which has three exponential components:

$$\begin{aligned} I(t) = {} & 6k^{\mathrm{F}} \frac{A_r}{(3\rho_r + 1)(4\rho_r + 1)} \exp\left(-\frac{6\rho_r + 3}{\tau} t\right) \\ & + 2k^{\mathrm{F}} \frac{B_r}{(2\rho_r + 1)(4\rho_r + 1)} \exp\left(-\frac{2\rho_r + 2}{\tau} t\right) \\ & + k^{\mathrm{F}} \frac{C_r}{(2\rho_r + 1)(3\rho_r + 1)} \exp\left(-\frac{1}{\tau} t\right) \quad \text{for } N = 3, \end{aligned} \tag{19}$$

where $A_r = \rho_r^2 P_{\Lambda_3}(0)$, $B_r = 3\rho_r(2\rho_r + 1)P_{\Lambda_3}(0) + \rho_r(4\rho_r + 1)P_{\Lambda_2}(0)$, and $C_r = 3(\rho_r + 1)(2\rho_r + 1)P_{\Lambda_3}(0) + 2(\rho_r + 1)(3\rho_r + 1)P_{\Lambda_2}(0) + (2\rho_r + 1)(3\rho_r + 1)$ $P_{\Lambda_1}(0)$. We show the shape of (19) in Fig. 3(b).

Furthermore, eigenvalue analysis using Maxima for the master equation (15) with the matrix $M$ for $N = 4$ (see inset in Fig. 3(c)) derives the fluorescence intensity decay of case $N = 4$ (where we avoid the long explicit formula for $M$), which has four exponential components:

$$\begin{aligned} I(t) = {} & 24k^{\mathrm{F}} \frac{A_r}{(4\rho_r + 1)(5\rho_r + 1)(6\rho_r + 1)} \exp\left(-\frac{12\rho_r + 4}{\tau} t\right) \\ & + 6k^{\mathrm{F}} \frac{B_r}{(3\rho_r + 1)(4\rho_r + 1)(6\rho_r + 1)} \exp\left(-\frac{6\rho_r + 3}{\tau} t\right) \\ & + 2k^{\mathrm{F}} \frac{C_r}{(2\rho_r + 1)(4\rho_r + 1)(5\rho_r + 1)} \exp\left(-\frac{2\rho_r + 2}{\tau} t\right) \\ & + k^{\mathrm{F}} \frac{D_r}{(2\rho_r + 1)(3\rho_r + 1)(4\rho_r + 1)} \exp\left(-\frac{1}{\tau} t\right) \quad \text{for } N = 4, \end{aligned} \tag{20}$$

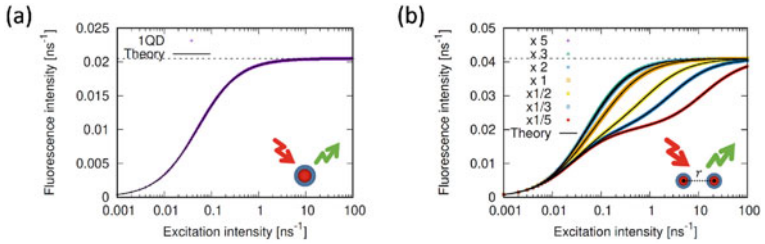


**Fig. 4** Nonlinearity in the multiple-donor model: (**a**) single-QD, and (**b**) two-QD situation. (**b**) Each color dot corresponding to each distance $r = \sqrt{c} \times R_0$, $c = 5, 3, 2, 1, 1/2, 1/3, 1/5$, respectively, where Förster distance $R_0 = 6.18$ nm

where $A_r = \rho_r^3 P_{\Lambda_4}(0)$, $B_r = 4\rho_r^2(3\rho_r + 1)P_{\Lambda_4}(0) + \rho_r^2(6\rho_r + 1)P_{\Lambda_3}(0)$, $C_r = 6\rho_r(2\rho_r + 1)(3\rho_r + 1)P_{\Lambda_4}(0) + 3\rho_r(2\rho_r + 1)(5\rho_r + 1)P_{\Lambda_3}(0) + \rho_r(4\rho_r + 1)(5\rho_r + 1)P_{\Lambda_2}(0)$, and $D_r = 4(\rho_r + 1)(2\rho_r + 1)(3\rho_r + 1)P_{\Lambda_4}(0) + 3(\rho_r + 1)(2\rho_r + 1)(4\rho_r + 1)P_{\Lambda_3}(0) + 2(\rho_r + 1)(3\rho_r + 1)(4\rho_r + 1)P_{\Lambda_2}(0) + (2\rho_r + 1)(3\rho_r + 1)(4\rho_r + 1)P_{\Lambda_1}(0)$. We show the shape of (20) in Fig. 3(c).

From the above specific results (17, 19, 20), we can infer the general case for $N \in \mathbb{N}$ that $\tau_*^{(N)} < \tau_*^{(N-1,1)} \leq \cdots \leq \tau_*^{(N-1,N)} < \tau$, that is, the network-induced decay times are shorter than the natural excited-state decay time $\tau$.

We show the nonlinearities of the multiple-donor model in the stationary excitation situation at the end of this subsection. First, considering the single QD case (see inset in Fig. 4(a)) with stationary excitation (the rate constant $k^{\mathrm{E}}$), the matrix $M$ in the case of $N = 1$ becomes

$$M = \frac{1}{\tau}\begin{bmatrix} -\tau k^{\mathrm{E}} & 1 \\ \tau k^{\mathrm{E}} & -1 \end{bmatrix} \quad \text{for } N = 1. \tag{21}$$

Eigenvalue analysis using Maxima for the master equation (15) with the matrix (21) derives the stationary fluorescence intensity of case $N = 1$:

$$I_{\mathrm{f}} = k^{\mathrm{F}} \frac{I_{\mathrm{e}}}{I_{\mathrm{e}} + (\sigma\tau)^{-1}} \quad \text{for } N = 1, \tag{22}$$

where $I_{\mathrm{e}} = \sigma^{-1}k^{\mathrm{E}}$ is the excitation intensity for the collision cross section $\sigma$. We show this nonlinearity between the fluorescence intensity $I_{\mathrm{f}}$ and the excitation intensity $I_{\mathrm{e}}$ in Fig. 4(a).

Next, considering the two-QD case (see inset in Fig. 4(b)) with stationary uniform excitation (the rate constant $k^{\mathrm{E}}$ for each QD), the matrix $M$ in the case of $N = 2$ becomes

$$M = \frac{1}{\tau}\begin{bmatrix} -2(\rho_r+1) & \tau k^{\mathrm{E}} & \tau k^{\mathrm{E}} & 0 \\ \rho_r+1 & -(\rho_r+1+\tau k^{\mathrm{E}}) & \rho_r & \tau k^{\mathrm{E}} \\ \rho_r+1 & \rho_r & -(\rho_r+1+\tau k^{\mathrm{E}}) & \tau k^{\mathrm{E}} \\ 0 & 1 & 1 & -2\tau k^{\mathrm{E}} \end{bmatrix} \quad \text{for } N=2, \tag{23}$$

where $\rho_r = (R_0/r)^6$, and $r$ is the distance between two QDs. Eigenvalue analysis using Maxima for the master equation (15) with the matrix (23) derives the stationary fluorescence intensity of case $N = 2$:

$$I_{\mathrm{f}} = 2k^{\mathrm{F}} \frac{I_{\mathrm{e}}^2 + \sigma^{-1}(\tau^{-1}\rho_r + \tau^{-1})I_{\mathrm{e}}}{I_{\mathrm{e}}^2 + 2\sigma^{-1}(\tau^{-1}\rho_r + \tau^{-1})I_{\mathrm{e}} + (\sigma\tau)^{-2}\rho_r + (\sigma\tau)^{-2}}, \tag{24}$$

where $I_{\mathrm{e}} = \sigma^{-1}k^{\mathrm{E}}$ is the excitation intensity for the collision cross section $\sigma$. We show this nonlinearity between the fluorescence intensity $I_{\mathrm{f}}$ and the excitation intensity $I_{\mathrm{e}}$ in Fig. 4(b). Note that the nonlinearity in Fig. 4(b) depends on the distance $r$ between two QDs and reveals an intermediate step as the distance $r$ decreases. The two-QD case result of (24) suggests that in a general QD network, the nonlinearity between fluorescence intensity (output) and excitation intensity (input) depends on the network structure complexity and has multiple distinct intermediate steps.

## 3 Simulation Methods

We can use either deterministic or stochastic approaches to simulate the multiple-donor model. Each method has its advantages and disadvantages.

### *3.1 Deterministic Simulation*

The deterministic approach numerically solves the master equation (4) as an initial value problem for a $2^N$-dimensional system of ordinary differential equations, for example, the Euler method and the Runge–Kutta method:

$$\begin{aligned} &\frac{\mathrm{d}}{\mathrm{d}t}\mathbf{P}(t) = \mathbf{F}(\mathbf{P}(t), t) \\ &\quad \text{or} \quad \frac{\mathrm{d}}{\mathrm{d}t}P_{i_1\ldots i_N}(t) = F_{i_1\ldots i_N}(\{P_{i_1\ldots i_N}(t)\}, t), \end{aligned} \tag{25}$$

where $\mathbf{P}(t) = (P_{1\ldots1}(t), P_{1\ldots0}(t), \ldots, P_{0\ldots0}(t))^{\mathsf{T}}$. The calculation time in the deterministic simulation increases exponentially with $2^N$ for the number of QDs, $N$. In the simulation with large $N$, the calculation of $F_{i_1\ldots i_N}$ dominates the whole calculation

**Algorithm 1** Calculate the value of $F_{i_1 \ldots i_N}$ in the right-hand side of (4)

**Input:** $t$, $(i_1, \ldots, i_N)$, and $\{P_{1\ldots1}(t), \ldots, P_{0\ldots0}(t)\}$
**Output:** $F_{i_1 \ldots i_N}(\{P_{i_1,\ldots,i_N}(t)\}, t)$
1: set $sum = 0$
2: **for** $n = 1, \ldots, N$ **do**
3: **if** $i_n = 1$ **then**
4: $sum = sum - (k_n^{\mathrm{F}} + k_n^{\mathrm{N}}) P_{i_1 \ldots i_N}(t) + k_n^{\mathrm{E}}(t) \mathcal{S}_n^- P_{i_1 \cdots i_N}(t)$
5: **for** $m = 1, \ldots, N$ **do**
6: $sum = sum - k_{nm}^{\mathrm{FRET}} P_{i_1 \ldots i_N}(t)$
7: **end for**
8: **else**
9: $sum = sum + (k_n^{\mathrm{F}} + k_n^{\mathrm{N}}) \mathcal{S}_n^+ P_{i_1 \ldots i_N}(t) - k_n^{\mathrm{E}}(t) P_{i_1 \ldots i_N}(t)$
10: **for** $m = 1, \ldots, N$ **do**
11: **if** $i_m = 1$ **then**
12: $sum = sum + k_{nm}^{\mathrm{FRET}} \left\{ \mathcal{S}_n^+ P_{i_1 \ldots i_N}(t) + \mathcal{S}_n^+ \mathcal{S}_m^- P_{i_1 \ldots i_N}(t) \right\}$
13: **end if**
14: **end for**
15: **end if**
16: **end for**

**Note**: This optimized algorithm was created by Dr. Jaehoon Yu (former associate professor at the Tokyo Institute of Technology).

time. Therefore, optimizing the calculation of $F_{i_1 \ldots i_N}$ is important to accelerate the deterministic simulation. We show an optimized algorithm for calculating $F_{i_1 \ldots i_N}$ in Algorithm 1, which reduces "if" conditional branches, "for" loops, and zero multiplications.

It is best to avoid using "if" conditional branches for GPU parallel computing. We transform the formula $F_{i_1 \ldots i_N}$ as follows for GPU parallelization:[1]

$$
\begin{aligned}
&F_{i_1 \ldots i_N}(\{P_{i_1,\ldots,i_N}(t)\}, t) = \\
&2 \sum_{n=1}^{N} \left( \frac{1}{2} - i_n \right) \left[ \left( k_n^{\mathrm{F}} + k_n^{\mathrm{N}} + \sum_{m=1}^{N} (i_n \oplus i_m) k_{nm}^{\mathrm{FRET}} \right) P_{i_1 \ldots 1 \ldots i_N}(t) - k_n^{\mathrm{E}}(t) P_{i_1 \ldots 0 \ldots i_N}(t) \right] \\
&+ \sum_{n,m=1}^{N} (1 - i_n) i_m \mathcal{S}_n^+ \mathcal{S}_m^- P_{i_1 \ldots i_N}(t). \qquad (26)
\end{aligned}
$$

This formula enables us to create an optimized algorithm that calculates $F_{i_1 \ldots i_N}$ without "if" conditional branches, which is suitable for GPU parallel computing. An algorithm optimized for GPU parallel computing will be created in future work.

[1] This transformed formula (26) was also created by Dr. Jaehoon Yu (former associate professor at the Tokyo Institute of Technology).

### 3.2 Stochastic Simulation

The stochastic approach generates a sample path of a stochastic process that obeys the master equation (4) by Gillespie's direct method (DM) [25], the first reaction method (FRM) [26], and the next reaction method (NRM) [27]. Consider one of the state transitions (2) in the multiple-donor model, say event $i$, and assume its rate constant is $k_i$. Then, the occurrence frequency per unit time, $a_i$, called "propensity," for the event $i$ is

$$a_1^{(n)} = i_n k_n^{\mathrm{F}} \quad (n = 1, \ldots, N), \tag{27a}$$

$$a_2^{(n)} = i_n k_n^{\mathrm{N}} \quad (n = 1, \ldots, N), \tag{27b}$$

$$a_3^{(n,m)} = i_n (1 - i_m) k_{nm}^{\mathrm{FRET}} \quad (n, m = 1, \ldots, N; n \neq m), \tag{27c}$$

$$a_4^{(n,m)} = i_n i_m k_{nm}^{\mathrm{FRET}} \quad (n, m = 1, \ldots, N; n \neq m), \tag{27d}$$

$$a_5^{(n)} = i_n k_n^{\mathrm{E}}(t) \quad (n = 1, \ldots, N). \tag{27e}$$

The total number of the above propensities $a_i$ is $3N + 2(N^2 - N) = 2N^2 + N$. However, we can reduce the total net number of propensities by integrating the third and fourth events:

$$a_1^{(n)} = i_n k_n^{\mathrm{F}} \quad (n = 1, \ldots, N), \tag{28a}$$

$$a_2^{(n)} = i_n k_n^{\mathrm{N}} \quad (n = 1, \ldots, N), \tag{28b}$$

$$a_{3\wedge 4}^{(n,m)} = i_n k_{nm}^{\mathrm{FRET}} \quad (n, m = 1, \ldots, N; n \neq m), \tag{28c}$$

$$a_5^{(n)} = i_n k_n^{\mathrm{E}}(t) \quad (n = 1, \ldots, N), \tag{28d}$$

where we can determine which third or fourth event occurs according to $i_m$ being 0 or 1. Therefore, the total number of propensities is reduced to $3N + (N^2 - N) = N^2 + 2N$. In the following, we write the propensities as $a_i$ $(i = 1, \ldots, N^2 + 2N)$ by flattening the above propensities $a_i^{(*)}$ of (28).

Gillespie-type algorithms are based on the fact that the waiting time $\tau_i$ until a subsequent event $i$ occurs follows an exponential distribution with a propensity, $P(\tau_i) = a_i e^{-a_i \tau_i}$ $(\tau_i > 0)$. The DM first generates a waiting time $\tau$ until *some* event occurs by an exponential distribution $P(\tau) = a e^{-a\tau}$ $(\tau > 0)$, where $a$ is the sum of propensities such that $a = \sum_i a_i$. After generating a waiting time $\tau$, which event occurred is determined according to the ratio of propensities $a_i$ (event $i$ is selected with probability $a_i/a$). Depending on the event that has occurred, the state $(i_1, \ldots, i_N)$ is changed, and the propensities $a_i$ are updated. We show a DM algorithm in Algorithm 2. We note that the DM does not assume time-dependent rate constants. Therefore, the DM cannot be adopted for the case of modulated excitation light, which includes time-dependent rate constants $k_n^{\mathrm{E}}(t)$.

The time-dependent rejection-based stochastic simulation algorithm (tRSSA) [28], one of the Gillespie-type algorithms, can handle time-dependent rate constants.

**Algorithm 2** Direct method (DM) [25] for the multiple-donor model (2)

**Input:** an initial state $\mathbf{x} = (i_1, \ldots, i_N)$
**Output:** a sample path $\{(t, \mathbf{x})\}$
1: initialize $t = 0$ with initial state $\mathbf{x}$
2: compute propensities $\{a_i\}$ according to the state $\mathbf{x}$
3: **while** $t < t_{\max}$ **do**
4: compute $a = \sum_i a_i$
5: generate a random number $r_1 \sim U(0, 1)$
6: compute waiting time $\tau = (-1/a) \ln r_1$
7: update time $t = t + \tau$
8: generate a random number $r_2 \sim U(0, 1)$
9: select minimum index $j$ s.t. $\sum_{i=1}^{j} a_i > r_2 a$
10: update state $\mathbf{x}$ depending on the selected event $j$
11: compute propensities $\{a_i\}$ according to the state $\mathbf{x}$
12: **end while**

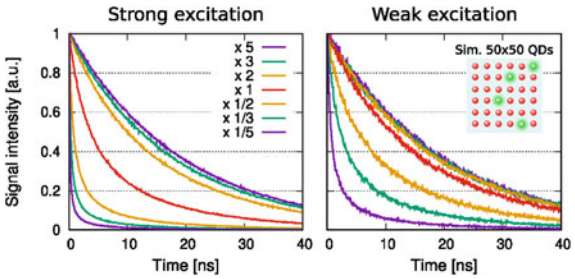


**Fig. 5** Simulation results from tRSSA [28] for slightly large FRET networks: $50 \times 50$ lattice arrangements. The solid lines represent the intensity data accumulated every 0.1 ns. The theoretically predicted features are found as follows: (i) the multicomponent exponential decay, (ii) fast decay in earlier times and slow decay in later times, and (iii) slower decay during higher dilution or lower excitation

The modified NRM (MNRM) [29], another Gillespie-type algorithm, can also handle time-dependent rate constants. However, the generation of the waiting time in the MNRM relies on the tractable calculation of the integration of the time-dependent rate constants and the solution of the inverse problem (see [28] for details). Furthermore, the tRSSA we adopted here is a computationally efficient and versatile Gillespie-type algorithm that does not rely on such tractable calculations and inverse problem solutions. In the following, we adopted the tRSSA for the case of modulated excitation light and also the case of constant excitation light. We show a tRSSA algorithm for the multiple-donor model in Algorithm 3.

Figure 5 shows the simulation results obtained from tRSSA described above for slightly large FRET networks. The simulation was conducted in the following settings: QDs were located on a $50 \times 50$ lattice, and the lattice spacing was $\sqrt{c} \times R_0$, where $c = 5$ to $1/5$, as shown in the legend. The parameters of QDs were set to $Q = 0.40$ (quantum yield), $\tau = 19.5$ ns (natural excited-state lifetime), and $R_0 = 6.18$ nm (Förster distance), assuming QD585. These QD parameters are used repeatedly

**Algorithm 3** The time-dependent RSSA (tRSSA) [28] for the multiple-donor model (2)

**Input:** an initial state $\mathbf{x} = (i_1, \ldots, i_N)$
**Output:** a sample path $\{(t, \mathbf{x})\}$
initialize $t = 0$ with initial state $\mathbf{x}$
define the bound $[\underline{\mathbf{x}}, \overline{\mathbf{x}}]$ as $\underline{x_i} = 0$ and $\overline{x_i} = x_i$ for $i = 1, \ldots, N$
discretize $[0, t_{\max}]$ to $k$ intervals $0 < t_1 < \cdots < t_k = t_{\max}$
set $i = 1$
compute propensity bounds $\{\underline{a_j}\}$ and $\{\overline{a_j}\}$ according to $\underline{\mathbf{x}}$ and $\overline{\mathbf{x}}$, respectively
compute $\overline{a} = \sum_j \overline{a_j}$
**while** $t < t_{\max}$ **do**
  generate a random number $r_1 \sim U(0, 1)$
  compute waiting time $\tau = (-1/a) \ln r_1$
  update time $t = t + \tau$
  **if** $t > t_i$ **then**
    set $t = t_i$
    update $i = i + 1$
    compute propensity bounds $\{\underline{a_j}\}$ and $\{\overline{a_j}\}$ according to $\underline{\mathbf{x}}$ and $\overline{\mathbf{x}}$, respectively
    go to 7
  **end if**
  generate two random numbers $r_2, r_3 \sim U(0, 1)$
  select minimum index $j$ s.t. $\sum_{k=1}^{j} a_k > r_2 a$
  set *accept* = **false**
  **if** $r_3 \leq \underline{a_j}/\overline{a_j}$ **then**
    set *accepted* = **true**
  **else**
    compute propensities $\{a_j\}$ according to current state $\mathbf{x}$
    **if** $r_3 \leq \underline{a_j}/\overline{a_j}$ **then**
      set *accepted* = **true**
    **end if**
  **end if**
  **if** *accepted* = **true then**
    update state $\mathbf{x}$ depending on the selected event $j$
    **if** $\mathbf{x} \in [\underline{\mathbf{x}}, \overline{\mathbf{x}}]$ **then**
      define a new bound $[\underline{\mathbf{x}}, \overline{\mathbf{x}}]$ around current state $\mathbf{x}$
      compute propensity bounds $\{\underline{a_j}\}$ and $\{\overline{a_j}\}$ according to $\underline{\mathbf{x}}$ and $\overline{\mathbf{x}}$, respectively
    **end if**
  **end if**
**end while**

in the following and are listed in Table 1. Furthermore, $\kappa^2$ (orientation factors) were set to $2/3$, assuming that our QD-experimental system is in the dynamic averaging regime for the three-dimensional spatial and orientational case (see Chap. 4 in [22] or [23] for effective kappa-squared values). In Fig. 5, "Strong excitation" and "Weak excitation" denote the initially excited QDs that account for 90% and 10% of the total amount, respectively. For simplicity, we assumed that QDs are points without volume in the simulation. We performed $10^4$ independent simulation trials and averaged the results. We accumulated photons in a time interval of 0.1 ns at each time point to evaluate the fluorescence intensity. We confirmed that the simulation results show

**Table 1** Simulation parameters assumed for QD585

| $Q$<br>Quantum yield | $\tau$<br>Natural excited-state lifetime | $R_0$<br>Förster distance | $\kappa^2$<br>Orientation factor |
|---|---|---|---|
| 0.40 | 19.5 ns | 6.18 nm | 2/3 |

multicomponent exponential decay. Specifically, the decays were fast in earlier times, slow in later times, and finally, with the natural decay time $\tau$, as stated above as the inference from the case $N = 2, 3, 4$. Moreover, the result shows faster decays as the density of excited QDs increases or the excitation becomes stronger, as expected due to the level occupancy effect. The effect promotes the emission of the transferred and saturated energy between excited QDs through a nonradiative process such as heat dissipation. As a result, the radiative energy dissipation becomes faster as the density of excited QDs increases or the excitation becomes strong (see also Sect. 4.1 in [11] for a more intuitive explanation).

### *3.3 Comparison Between Deterministic and Stochastic Simulation*

We compare deterministic and stochastic simulations to understand the difference in characteristics. We assume common QD parameters, as shown in Table 1. We further assume a 4QD $2 \times 2$ lattice arrangement system, where the nearest neighbor distance is $R_0$, and the 4QD system consists of single-type QDs. In the following, the time step of the Runge–Kutta method in the deterministic simulation is set to 0.01 ns. Meanwhile, in the stochastic simulation, the fluorescence photon accumulation time is set to 0.1 ns, and the sampling number repeated for averaging is set to $10^6$.

Figure 6 compares deterministic and stochastic simulations for the 4QD system with no excitation light situation. The obtained normalized fluorescence intensity decays are nearly identical, but the stochastic one includes small noises due to the intrinsic probabilistic nature of FRET. Figure 7 compares deterministic and stochastic simulations for the 4QD system with sinusoidal excitation light: $k^{\mathrm{E}}(t) = A(1 + \varepsilon \sin(2\pi t/T))$, $A = 1\ \mathrm{nm}^{-1}$, $\varepsilon = 0.8$, and $T = 5$ ns. The obtained modulated fluorescence intensities are nearly identical even under excitation light, and the stochastic one includes small noises due to the FRET intrinsic probabilistic nature. Figure 8 compares deterministic and stochastic simulations for the 4QD system with rectangular excitation light: $k^{\mathrm{E}}(t) = A\theta(t_w - (t \mod T))$, $A = 1\ \mathrm{nm}^{-1}$, $t_w = 1$ ns, and $T = 5$ ns, where $\theta(t)$ is the Heaviside function. The obtained modulated fluorescence intensities are also almost identical to the above cases, and the stochastic one again includes small noises due to the FRET intrinsic probabilistic nature.

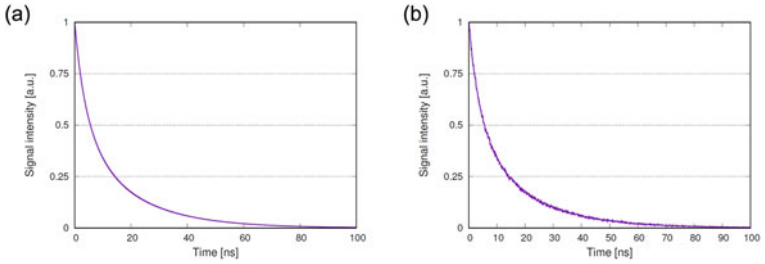


**Fig. 6** Comparison of (**a**) deterministic and (**b**) stochastic simulations in the no excitation light situation for the 4QD 2 × 2 lattice arrangement system

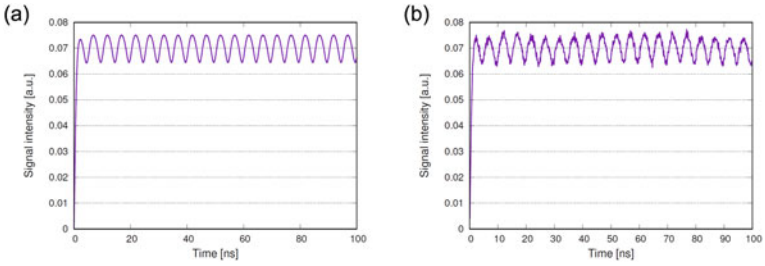


**Fig. 7** Comparison of (**a**) deterministic and (**b**) stochastic simulations in the sinusoidal excitation light situation for the 4QD 2 × 2 lattice arrangement system

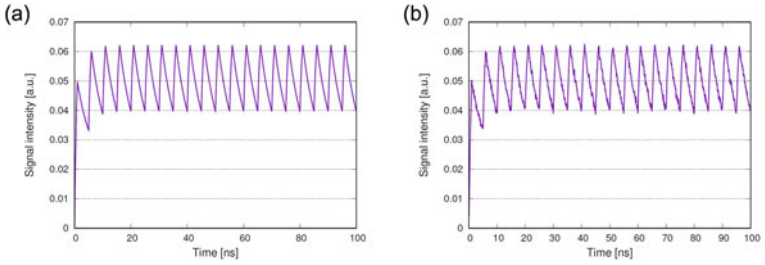


**Fig. 8** Comparison of (**a**) deterministic and (**b**) stochastic simulations in the rectangular excitation light situation for the 4QD 2 × 2 lattice arrangement system

The above three cases suggest that the stochastic simulation results converge to the deterministic simulation results in the limit of large sampling numbers. A large sampling number is required for a clear result in stochastic simulations. Nonetheless, noises in stochastic simulations are faithful to actual observations. Therefore, the sampling number in the stochastic simulation is determined by the considered situations.

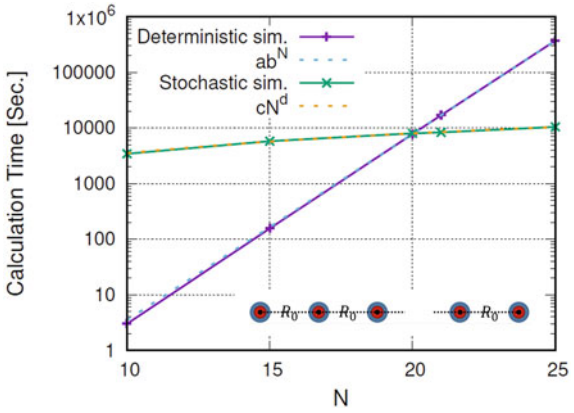


**Fig. 9** Comparison of calculation times between deterministic and stochastic simulations. The network structure is chain-like, as shown in the bottom inset

**Table 2** Pros and cons of deterministic and stochastic simulations

| Deterministic simulation | Stochastic simulation |
|---|---|
| Merits<br>• Fewer QDs means faster calculations<br>• Clear results are obtained | Merits<br>• Calculation time does not increase significantly even if the number of QDs increases<br>• Noises are faithful to actual observations |
| Demerits<br>• Calculation time increases exponentially if the number of QDs increases<br>• It is necessary to investigate the influence of intrinsic noise separately | Demerits<br>• Fewer QDs take longer calculation time than deterministic simulation<br>• Evaluation of the results must be careful since inherent noise is always included |

Finally, we show the trade-off nature between deterministic and stochastic simulations. Figure 9 represents the calculation times of deterministic and stochastic simulations in the case of chain-like networks. As shown in Fig. 9, deterministic simulations are appropriate for small-number situations. However, the calculation times of deterministic simulations increase exponentially as the number of QDs increases. On the other hand, the calculation times of stochastic simulations increase polynomially as the number of QDs increases. Therefore, the calculation times between stochastic and deterministic simulations reverse at some number of QDs. Table 2 summarizes the pros and cons of deterministic and stochastic simulations.

## 4 Information Processing Using FRET Networks

In this section, we show the power of FRET networks for information processing. This section follows our previous studies [30, 31]. As shown in Fig. 10(a), our information processing scheme has a standard structure with an input layer, a single hidden layer (consisting of FRET networks), and an output layer. The parameters to be trained are only output weights (the part of readout) connecting the hidden and output layers, such as reservoir computing. We sometimes call this hidden layer the "FRET-network reservoir." Feedback in Fig. 10(a) is optional for an autonomous signal generation or increased memory. The learning method used for the output weights is linear regression, particularly ridge regression, which is similar to reservoir computing.

Here, we assume a working hypothesis for the simulator's limited ability:

1. Each node consists of infinitely many two-QD pairs.
2. There are no interactions between such pairs.

The working hypothesis is not essential for information processing. It is only due to the simulator's limited memory, processing speed, etc. The working hypothesis implies that fluorescence from each node is free from inherent noise, which enables us to perform the deterministic simulation using Algorithm 1 with $N = 2$ for each node. Therefore, the simulation becomes low-cost and suitable for CPU-thread or GPU parallelization. We assume that FRET networks consist of QD585 and the simulation parameters of FRET networks are listed in Table 1.

We further assume a standard input scheme called the time-piecewise constant excitation, as shown in Fig. 10(b). The time-piecewise constant excitation has stationary excitation intensity within an excitation duration $[t_p, t_p + \Delta t)$ and switches to another excitation intensity just before the next excitation duration $[t_p + \Delta t, t_p + 2\Delta t)$. The fluorescence of each node is briefly observed just before the excitation switches. Therefore, the excitation switching time $\Delta t$ equals the fluorescence sampling time. As shown in Fig. 10(b), the smaller the excitation switching time $\Delta t$, the more past inputs reflect the output. Thus, the excitation switching time and the memory in the reservoir are negatively correlated. We finally assume that

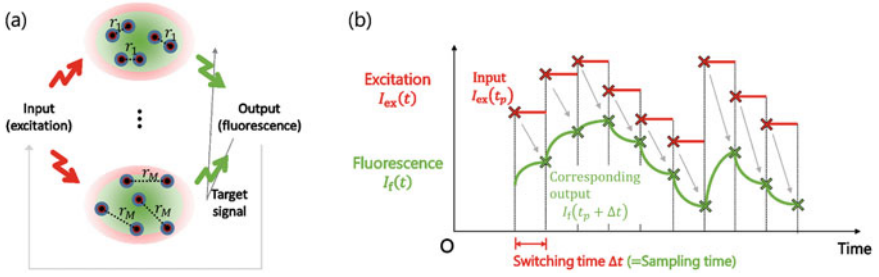


**Fig. 10** FRET-network reservoir: (**a**) Fundamental network structure with optional feedback, (**b**) Input scheme by time-piecewise constant excitation

the excitation intensity is created from an exponentially enhanced input signal as follows:

$$I_{\mathrm{ex}} = 10^{su_{\mathrm{input}}+b}, \tag{29}$$

where $s$ and $b$ are a scale factor and a bias constant, respectively. The scale factor $s$ and bias constant $b$ are set such that the dynamic range of the excitation intensity $I_{\mathrm{ex}}$ is within a significant change region in the nonlinearity, approximately [0.01, 100], as seen in Fig. 4(b).

## *4.1 Nonlinear Function Approximation*

We show the ability of FRET networks for nonlinear function approximation [30]. The goal of the task is to learn the nonlinear transformation $u(t) \mapsto y(t) = \frac{1}{2}\{u(t)\}^7$ through input–output relation data $\{(\sin(t/5), \frac{1}{2}\sin^7(t/5))\}_{t=0,\Delta t,2\Delta t,\cdots,n\Delta t}$. The training and prediction phases are performed with no feedback. Since this task needs no memory, the excitation switching time $\Delta t$ should be set large. Here we set the excitation switching time $\Delta t = 100$ ns.

Figure 11 represents the result of this nonlinear function approximation. Training is done by the first half of 100 input–output data (until $t = 10000$ ns), and prediction is performed by the following 100 input data (from $t = 10000$ ns until $t = 20000$ ns). Other simulation settings are as follows: the number of nodes is set to $N_{\mathrm{net}} = 1000$, the distance between each two-QD pair is chosen between minimum $r_{\mathrm{min}} = 0.3R_0$ nm and maximum $r_{\mathrm{max}} = 2.0R_0$ nm, the scale factor and bias constant is set to $s = 1.0$ and $b = 0.0$, respectively, and the regularization factor for the ridge regression is set to $\lambda = 10^{-10}$. We set the transient duration to 80 ns to ignore the transient behaviors of the reservoir.

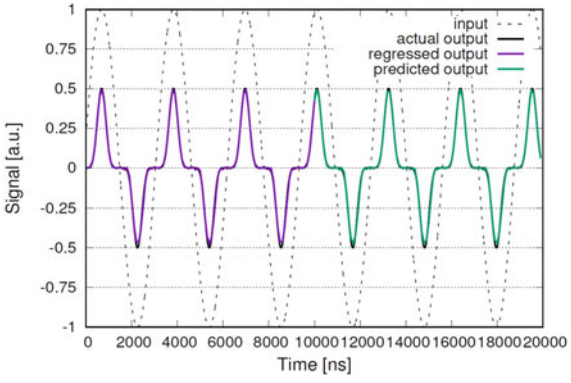


**Fig. 11** Nonlinear function approximation: input $u(t) = \sin(t/5) \mapsto$ output $y(t) = \frac{1}{2}\sin^7(t/5)$

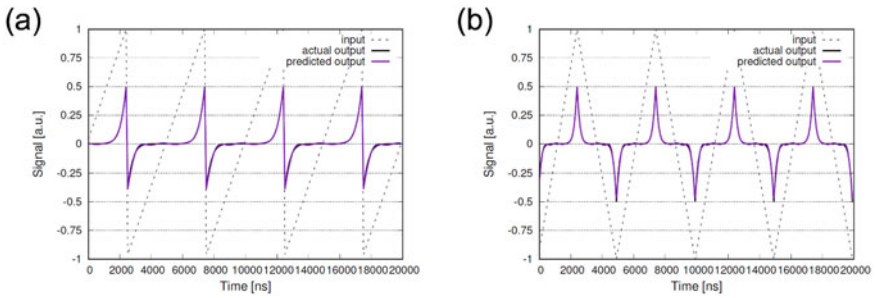


**Fig. 12** Generalization of nonlinear function approximation $\tilde{u}(t) \mapsto \tilde{y}(t) = \frac{1}{2}\tilde{u}(t)^7$ using different input data from the original one $\sin(t/5)$, (**a**) a sawtooth wave and (**b**) a triangle wave. The prediction is performed with the pre-trained weight by $u(t) = \sin(t/5) \mapsto y(t) = \frac{1}{2}\sin^7(t/5)$

Furthermore, we check the generalization of this nonlinear function approximation using different input data from the original one. Figure 12 shows the results. The prediction is performed with the pre-trained weight by the original input–output data. The predicted outputs become $\tilde{y}(t) = \frac{1}{2}\tilde{u}(t)^7$ in both cases, (a) sawtooth input wave and (b) triangle input wave. These results mean that the nonlinear function approximation is certainly generalized.

## *4.2 Chaotic Time-Series Prediction*

We demonstrate the capability of FRET networks for chaotic time-series prediction with minimal memory requirements [30]. The goal of the task is to predict the next step of the Hénon map, $x_{n+1} = 1 - 1.4x_n^2 + 0.3x_{n-1}$, from the present step $x_n$ with a memory of the past $x_{n-1}$ left in the reservoir. This task imposes the use of memory in the reservoir. Therefore, the prediction phase is performed with feedback, as shown in Fig. 10(a). On the other hand, the training phase is performed with no feedback. Since this task needs some memory, the excitation switching time $\Delta t$ should be moderately small. Here, we set the excitation switching time $\Delta t = 0.5$ ns.

Figure 13 represents the result of this chaotic time-series prediction. Training is done by the first half of 100 input–output data (until $t = 50$ ns), and prediction is performed by the following 100 input data (from $t = 50$ ns to $t = 100$ ns). Other simulation settings are as follows: the number of nodes is set to $N_{\text{net}} = 1000$, the distance between each two-QD pair is chosen between minimum $r_{\min} = 0.3R_0$ nm and maximum $r_{\max} = 2.0R_0$ nm, the scale factor and bias constant is set to $s = 1/3 + 0.1\xi$ and $b = 0.5 + 0.1\eta$ (where $\xi$, $\eta$ are uniform random numbers in $[-1, 1]$), respectively, and the regularization factor for the ridge regression is set to $\lambda = 10^{-10}$. We set the transient duration to 40 ns to ignore the transient behaviors of the reservoir.

Furthermore, we check the attractor reconstruction made from the above chaotic time-series prediction. Figure 14 shows the result. Each cross point (green) in the

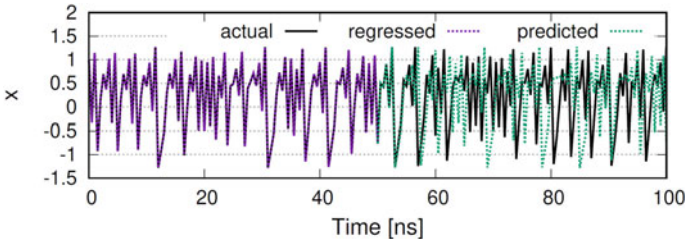


**Fig. 13** Chaotic time-series prediction for the Hénon map

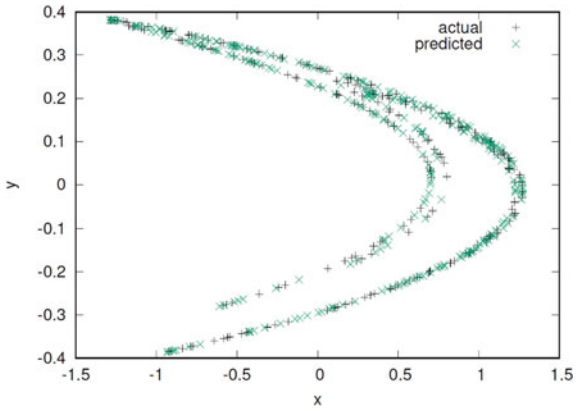


**Fig. 14** Reconstructed strange attractor of the Hénon map from the predicted time series

figure denotes $(x_n, x_{n+1})$ made from the predicted time series in the above task. This result means that the Hénon map's strange attractor is certainly reconstructed.

Finally, we evaluate the performance of the chaotic time-series prediction by the root mean square error (RMSE), which is defined as $\mathrm{RMSE} = \sqrt{\frac{1}{N}\sum_{n=1}^{N}\langle(x_n - \tilde{x}_n)^2\rangle}$, where $x_n, \tilde{x}_n$ are actual and predicted time series, respectively, and $\langle\cdot\rangle$ is the average with respect to different initial conditions (note: initial conditions for $x_n$ and $\tilde{x}_n$ are set to equal). Figure 15 shows RMSE versus (a) step $n$ from the start of prediction and (b) the excitation switching time $\Delta t$. The excitation switching time $\Delta t = 0.5$ ns provides the best performance in this task as it has the smallest RMSE. This result means that this task needs appropriate memory. Thus, a large excitation switching time $\Delta t$ reduces available memory, whereas a small excitation switching time $\Delta t$ disrupts prediction by introducing unnecessary memory.

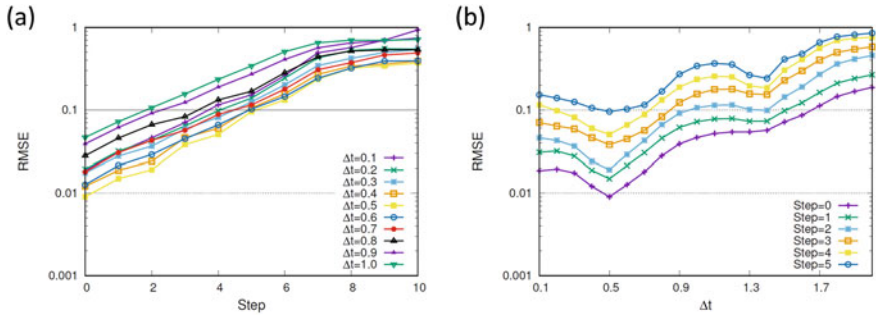


**Fig. 15** Root mean square error (RMSE) versus (**a**) step $n$ from the start of prediction and (**b**) excitation switching time $\Delta t$

## *4.3 Handwritten Digit Recognition*

We show the ability of FRET networks for pattern recognition, particularly handwritten digit recognition [31]. The goal of the task is to classify handwritten digit images to correct digits using the MNIST handwritten digit dataset. Figure 16 depicts our pattern recognition scheme. Since this task needs no memory, the training and prediction phases are performed with no feedback, and the excitation switching time $\Delta t$ should be set large. Here, we set the excitation switching time $\Delta t = 100$ ns as in the nonlinear function approximation.

We note that an input weight matrix is needed to transform an image vector $\mathbf{x}$ to an excitation intensity vector $\mathbf{I}_{\text{ex}}$. The image vector $\mathbf{x}$ and excitation intensity vector $\mathbf{I}_{\text{ex}}$ are $N_i$ $(= 784)$ and $N_{\text{net}}$ dimensional, respectively. Therefore, the input weight matrix $V$ has $N_{\text{net}}$ rows and $N_i$ columns such that $\mathbf{I}_{\text{ex}} = 10^{sV\mathbf{x}+b}$. The input

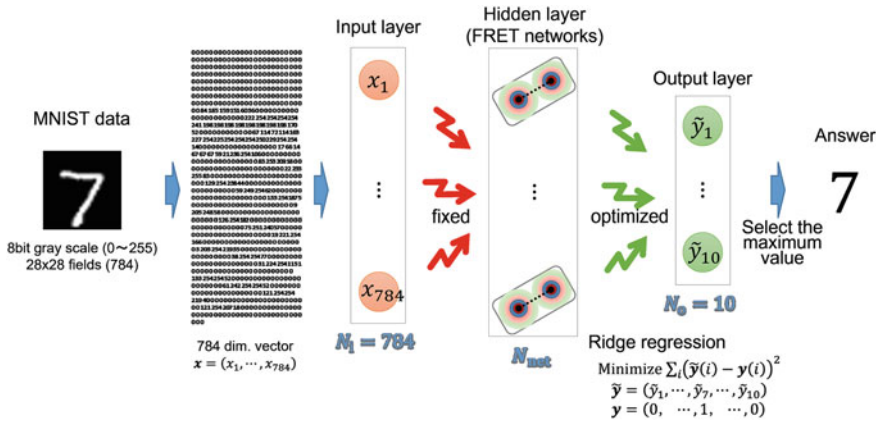


**Fig. 16** Pattern recognition scheme using FRET networks

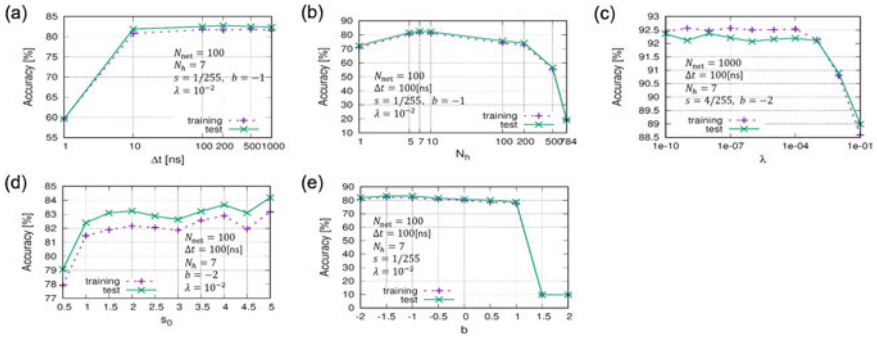


**Fig. 17** Investigation of appropriate hyperparameters for MNIST handwritten digit recognition. Investigated hyperparameters are (**a**) excitation switching times $\Delta t$, (**b**) the number of nonzero elements $N_h$ per row in the input weight matrix, (**c**) regularization parameters for ridge regression $\lambda$, (**d**) scale factors for excitation intensity $s_0$, and (**e**) bias constants for excitation intensity $b$

weight matrix $V$ is better sparse. Therefore, the number of nonzero elements $N_h$ per row is also better small. We randomly select the nonzero elements and set the sum of elements per row to one in the input weight matrix.

We first investigate appropriate hyperparameters, as shown in Fig. 17. The evaluation uses accuracy for the MNIST handwritten digit dataset with training data of 60000 and test data of 10000. Investigated hyperparameters are (a) excitation switching times $\Delta t$, (b) the number of nonzero elements $N_h$ per row in the input weight matrix, (c) regularization parameters for ridge regression $\lambda$, (d) scale factors for excitation intensity $s_0$, and (e) bias constants for excitation intensity $b$. This investigation shows that (a) $\Delta t$ should be large to some extent, (b) $N_h$ should be approximately $1/100$ of the total, (c) $\lambda$ should be small to some extent, and (d, e) $s$ and $b$ should be set such that the dynamic range of the excitation intensity is within the nonlinear region. The adopted hyperparameters are as follows: the excitation switching time is set to $\Delta t = 100$ ns, the number of nonzero elements per row in the input weight matrix is set to $N_h = 7$, the regularization factor for the ridge regression is set to $\lambda = 10^{-4}$, and the scale factor and bias constant is set to $s = 4/255$ and $b = -2$, respectively. The distance between each two-QD pair is chosen between minimum $r_{\min} = 0.3R_0$ nm and maximum $r_{\max} = 1.0R_0$ nm. In the task, we set no transient duration.

Figure 18 shows the main result of MNIST handwritten digit recognition: accuracy versus the number of FRET-network nodes. The accuracy is 92% in the case of $N_{\text{net}} = 1000$, 94% in the case of $N_{\text{net}} = 2000$, and finally reaches approximately 95% in the case of $N_{\text{net}} = 3000$. This accuracy is almost as good as the ELM-based MNIST handwritten digit recognition accuracy of 94% in the case of 1000 nodes (see Table 1 in [32]).

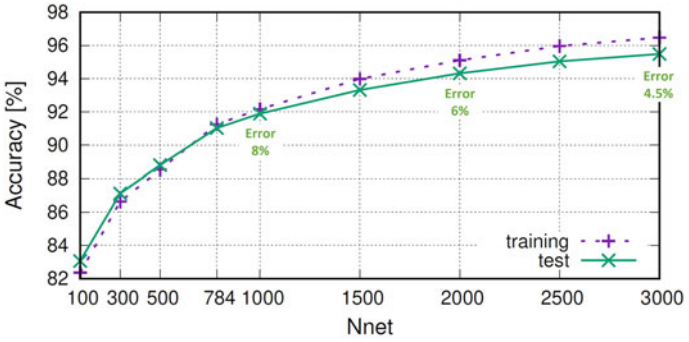


**Fig. 18** Dependence of accuracy on the number of FRET-network nodes in MNIST handwritten digit recognition

## 5 Conclusions and Future Works

In this chapter, we first introduced a spatiotemporal model for FRET networks, called the multiple-donor model, and showed various analytical (theoretical) results. The derivation of network-induced multicomponent exponential decay and the analytical results for small QD systems, including the nonlinear relation between input excitation intensity and output fluorescence intensity, are demonstrated. We then presented the deterministic and stochastic simulation methods for FRET networks and compared their advantages and disadvantages. In general, deterministic simulations are appropriate for only a few QDs situations, whereas stochastic simulations are appropriate for many QDs situations in terms of computational costs. We finally showed the power of FRET networks for information processing by simulations, particularly nonlinear function approximation, chaotic time-series prediction, and MNIST handwritten digit recognition.

We are considering future work on reinforcement learning using FRET networks and spatial network design theory. Reinforcement learning is one of the important applications for FRET networks. We believe that the ability of FRET networks to recognize patterns and predict chaotic time series (with some memory) provides the power for reinforcement learning. On the other hand, the power of FRET networks would be maximized if the spatial network (spatial arrangement of QDs) were appropriately optimized. We currently lack a design theory for the spatial network of QDs. Therefore, developing spatial network design theory is an urgent issue for realizing novel information processing devices.

**Acknowledgements** I would like to thank my colleagues, especially Dr. Naoya Tate (Kyushu University) and Dr. Jaehoon Yu (former Tokyo Institute of Technology), for their valuable comments. This study is supported by JST CREST Grant Number JPMJCR18K2, Japan. Finally, I would like to express my deepest gratitude and love to my late mother, Junko Nakagawa (March 1953–January 2023), who gave me birth, raised me, and watched over my life.

## References


1. J.R. Lakowicz, *Principles of Fluorescence Spectroscopy*, 3rd edn. (Springer, Boston, MA, 2006). https://doi.org/10.1007/978-0-387-46312-4
2. T. Nishimura, Y. Ogura, J. Tanida, Fluorescence resonance energy transfer-based molecular logic circuit using a DNA scaffold. Appl. Phys. Lett. **101**, 233703 (2012). https://doi.org/10.1063/1.4769812
3. C.D. LaBoda, A.R. Lebeck, C.L. Dwyer, An optically modulated self-assembled resonance energy transfer pass gate. Nano Lett. **17**, 3775–3781 (2017). https://doi.org/10.1021/acs.nanolett.7b01112
4. M. Massey, I.L. Medintz, M.G. Ancona, W.R. Algar, Time-gated FRET and DNA-based photonic molecular logic gates: AND, OR, NAND, and NOR. ACS Sens. **2**, 1205–1214 (2017). https://doi.org/10.1021/acssensors.7b00355
5. J. Inoue, T. Nishimura, Y. Ogura, J. Tanida, Nanoscale optical logic circuits by single-step FRET. IEEE Photonics J. **12**, 6500112 (2020). https://doi.org/10.1109/JPHOT.2020.2976489
6. C.M. Spillmann, S. Buckhout-White, E. Oh, E.R. Goldman, M.G. Anconac, I.L. Medintz, Extending FRET cascades on linear DNA photonic wires. Chem. Commun. **50**(55), 7246–7249 (2014). https://doi.org/10.1039/c4cc01072h
7. S. Vyawahare, S. Eyal, K.D. Mathews, S.R. Quake, Nanometer-scale fluorescence resonance optical waveguides. Nano Lett. **4**(6), 1035–1039 (2004). https://doi.org/10.1021/nl049660i
8. K.F. Chou, A.M. Dennis, Förster resonance energy transfer between quantum dot donors and quantum dot acceptors. Sensors **15**, 13288–13325 (2015). https://doi.org/10.3390/s150613288
9. N. Kholmicheva, P. Moroz, H. Eckard, G. Jensen, M. Zamkov, Energy transfer in quantum dot solids. ACS Energy Lett. **2**, 154–160 (2017). https://doi.org/10.1021/acsenergylett.6b00569
10. V. Nellore, S. Xi, C. Dwyer, Self-assembled resonance energy transfer keys for secure communication over classical channels. ACS Nano **9**, 11840–11848 (2015). https://doi.org/10.1021/acsnano.5b04066
11. S. Shimomura, T. Nishimura, Y. Miyata, N. Tate, Y. Ogura, J. Tanida, Spectral and temporal optical signal generation using randomly distributed quantum dots. Opt. Rev. (2020). https://doi.org/10.1007/s10043-020-00588-7. (March)
12. M. Nakagawa, Y. Miyata, N. Tate, T. Nishimura, S. Shimomura, S. Shirasaka, J. Tanida, H. Suzuki, Spatiotemporal model for fret networks with multiple donors and acceptors: multicomponent exponential decay derived from the master equation. J. Opt. Soc. Am. B **38**(2), 294–299 (2021). https://doi.org/10.1364/josab.410658
13. M. Naruse, N. Tate, M. Aono, M. Ohtsu, *Nanointelligence: Information Physics Fundamentals for Nanophotonics*, Chapter 1 (Springer, Berlin, Heidelberg, 2014), pp. 1–39 . https://doi.org/10.1007/978-3-642-40224-1_1
14. N. Tate, M. Naruse, W. Nomura, T. Kawazoe, T. Yatsui, M. Hoga, Y. Ohyagi, Y. Sekine, H. Fujita, M. Ohtsu, Demonstrate of modulatable optical near-field interactions between dispersed resonant quantum dots. Opt. Express **19**, 18260–18271 (2011). https://doi.org/10.1364/OE.19.018260
15. M. Naruse, P. Holmström, T. Kawazoe, K. Akahane, N. Yamamoto, L. Thylén, M. Ohtsu, Energy dissipation in energy transfer mediated by optical near-field interactions and their interfaces with optical far-fields. Appl. Phys. Lett. **100**, 241102 (2012). https://doi.org/10.1063/1.4729003
16. M. Naruse, M. Aono, S.-J. Kim, T. Kawazoe, W. Nomura, H. Hori, M. Hara, M. Ohtsu, Spatiotemporal dynamics in optical energy transfer on the nanoscale and its application to constraint satisfaction problems. Phys. Rev. B **86**, 125407 (2012). https://doi.org/10.1103/PhysRevB.86.125407
17. S. Wang, A.R. Lebeck, C. Dwyer, Nanoscale resonance energy transfer-based devices for probabilistic computing. IEEE Micro **35**, 72–84 (2015). https://doi.org/10.1109/MM.2015.124

18. S. Wang, R. Vyas, C. Dwyer, Fluorescent taggants with temporally coded signatures. Opt. Express **24**(14), 15528–15545 (2016). https://doi.org/10.1364/OE.24.015528
19. C. Berney, G. Danuser, FRET or No FRET: a quantitative comparison. Biophys. J. **84**, 3992–4010 (2003). https://doi.org/10.1016/S0006-3495(03)75126-1
20. C. Dwyer, A. Rallapalli, M. Mottaghi, S. Wang, *DNA Self-Assembled Nanostructures for Resonance Energy Transfer Circuits*, Chapter 2 (Springer, Berlin, Heidelberg, 2014), pp. 41–65. https://doi.org/10.1007/978-3-642-40224-1_2
21. M.T. Trinh, R. Limpens, T. Gregorkiewicz, Experimental investigations and modeling of auger recombination in silicon nanocrystals. J. Phys. Chem. C **117**, 5963–5968 (2013). https://doi.org/10.1021/jp311124c
22. I.L. Medintz, N. Hildebrandt, *FRET-Förster Resonance Energy Transfer: From Theory to Applications*, 1st edn. (Wiley, New York, 2013). https://doi.org/10.1002/9783527656028
23. R.E. Dale, J. Eisinger, W.E. Blumberg, The orientational freedom of molecular probes. the orientation factor in intramolecular energy transfer. Biophys. J. **26**(2), 161–193 (1979). https://doi.org/10.1016/S0006-3495(79)85243-1
24. D.D. Thomas, W.F. Carlsen, L. Stryer, Fluorescence energy transfer in the rapid-diffusion limit. Proc. Natl. Acad. Sci. **75**(12), 5746–5750 (1978). https://doi.org/10.1073/pnas.75.12.5746
25. D.T. Gillespie, Exact stochastic simulation of coupled chemical reactions. J. Phys. Chem. **81**(25), 2340–2361 (1977). https://doi.org/10.1021/j100540a008
26. D.T. Gillespie, General method for numerically simulating stochastic time evolution of coupled chemical-reactions. J. Comput. Phys. **22**(4), 403–434 (1976). https://doi.org/10.1016/0021-9991(76)90041-3
27. M.A. Gibson, J. Bruck, Efficient exact stochastic simulation of chemical systems with many species and many channels. J. Phys. Chem. A **104**(9), 1876–1889 (2000). https://doi.org/10.1021/jp993732q
28. V.H. Thanh, C. Priami, Simulation of biochemical reactions with time-dependent rates by the rejection-based algorithm. J. Chem. Phys. **143**, 054104 (2015). https://doi.org/10.1063/1.4927916
29. F. Anderson, A modified next reaction method for simulating chemical systems with time dependent propensities and delays. J. Chem. Phys. **127**(21), 214107 (2007). https://doi.org/10.1063/1.2799998
30. M. Nakagawa, Y. Miyata, N. Tate, T. Nishimura, S. Shimomura, S. Shirasaka, J. Tanida, H. Suzuki, Modeling and analysis of fret networks: toward development of novel information processing devices, in *Proceedings of the 2020 International Symposium on Nonlinear Theory and its Applications (NOLTA2020), The Institute of Electronics, Information and Communication Engineers (IEICE)* (Tokyo, Japan, 2020), pp. 217–220
31. M. Nakagawa, Pattern recognition using fret networks: a preliminary study, in *Proceedings of the 2022 International Symposium on Nonlinear Theory and its Applications (NOLTA2022), The Institute of Electronics, Information and Communication Engineers (IEICE)* (Tokyo, Japan, 2022), p. 131
32. M.D. McDonnell, M.D. Tissera, T. Vladusich, A. van Schaik, J. Tapson, Fast, simple and accurate handwritten digit classification by training shallow neural network classifiers with the "extreme learning machine algorithm. PLoS ONE **10**(8), e0134254 (2015). https://doi.org/10.1371/journal.pone.0134254